Synchrotron X-ray and Crystal Morphology Control in Biodegradable Polymer Blends

Y. A. Akpalu, J. C. Meredith, and E. J. Amis
National Institute of Standards & Technology

Although few biological tissues are homogeneous, single-component materials, tissue scaffolds are often made from brittle biodegradable aliphatic polyester foams [1-3]. Typically poly(lactic acid), poly(glycolic acid), poly(lactic acid-co-glycolic acid) and other copolymers of lactic acid are used [2,3]. Poly(e-caprolactone) (PCL) is a biodegradable polymer that has also received increasing interest from the scientific and medical communities [4,5]. Blending PCL (an elastomer) with amorphous poly(D,L-lactic acid) (PDLA, a brittle polymer) may offer a simple and cost-effective method of achieving a range of mechanical properties that is similar to many load bearing tissues. The advantage of blending is that melt phase separation can be used to create a rich range of morphologies if the polymer sample is quenched from a one-phase state to a two-phase state [6,7]. However, the successful application of polymer blend requires detailed knowledge of how melt phase separation and subsequent crystallization affect the morphology. In crystal-amorphous blends, the crystal morphology depends on the segregation of the noncrystallizable components into the interlamellar, interfibrillar and interspherulitic regions, as shown in Figure 1. When melt phase separation occurs before crystallization, the presence of a phase rich in amorphous material can affect each type of segregation (liquid-liquid and liquid-solid) and hence the crystal morphology.

In this highlight, the effect of melt phase separation on the crystallization of PCL/PDLA blends is studied by real-time simultaneous small-angle x-ray scattering (SAXS) and wide-angle x-ray scattering (WAXS) at beamline X27C at the NSLS. The previously determined [8] cloud point curve (melt phase diagram) for the PCL/PDLA samples used in our studies indicates a lower solution critical temperature (LCST) of 86 °C and a critical concentration of mass fraction 36 % PCL. Since the LCST temperature (T_{LCST} = 86 °C) of PCL/PDLA is greater than the melting temperature (60 °C) of PCL, these blends offer an opportunity to independently study the effect of melt phase separation and blending on crystallization. In addition, relatively short annealing times in the two-phase region (0 hours to 2 hours) are needed to study how the size of the phase separated domains affect crystallization. Morphological parameters that characterize the nanoscale crystal morphology can be obtained directly by simultaneous SAXS/WAXS. To the best of our knowledge, this is the first use of simultaneous SAXS/WAXS to investigate the effect of melt phase separation on the crystallinity and segregation of noncrystallizable components (amorphous PDLA and uncrystallized PCL) in a blend where T_g(blend) < T_m < T_{LCST}.

For the SAXS data presented in this work, the average size of the lamellar stack (ξ_L = 48 nm) is much smaller than the size (63 nm) of the largest structure that can be resolved in the scattering profile. Hence, the scattering arising from the contrast between the lamellar stacks (x_L) and the surrounding noncrystalline regions (1- x_L) contributes to the total scattering observed. Structural changes occurring at characteristic length scales of 20 nm to 63 nm were resolved in SAXS while those at 0.1 nm to 1 nm were resolved in WAXS. In order to obtain variables that characterize the interlamellar and interfibrillar morphology (Figure 1) we perform a correlation function analysis [9-11] and an intensity model analysis [12]. Both methods give estimates for the lamellar spacing (L = 17 nm), the average interlayer amorphous thickness (l_a = 7 nm) and the average crystal thickness (l_c = 10 nm). However, ξ_L and the average amorphous spacing between stacks (L_D = 29 nm) can only be obtained from the intensity model. From these parameters $x_L = \xi_L/(\xi_L + L_D)$ (intensity model), $x_{CL} = l_c/L$ (correlation function) and $x_{CL} = L - l_a/L$ (intensity model).

In order to discuss structural changes from our measurements it is convenient to employ the SAXS invariant (Q) defined as $Q = I(q)q^2dq$ [13] and the crystal-

linity from WAXS (w_c) [14,15]. For most purposes, the experimental contribution to the SAXS invariant (Q_{SAXS}) can be used to characterize structure development [11,16,17]. Since Q_{SAXS} and w_c can be written in terms x_S, x_L and x_{CL} (Figure 1), these quantities can be used to monitor how melt phase separation affects the crystal morphology. Mathematical expressions for Q_{SAXS} and w_c are given by the following equations:

$$Q_{SAXS} = Cw_c(1-w_c)(\Delta\rho)^2 / D_\rho \quad (1)$$

$$w_c = D_\rho(x_s x_L x_{CL} + \Phi_D) \quad (2)$$

$$\Delta\rho = \rho_c - (\varphi_{a,PCL}\rho_{a,PCL} + \varphi_{a,PDLA}\rho_{a,PDLA}) \quad (3)$$

In Equations 1 and 2, D_ρ, the factor used to convert mass fractions to volume fractions, is close to 1 for most polymers. C is a constant related to the specific experimental apparatus and Φ_D is the volume fraction of crystals in the interfibrillar and interspherulitic regions. The electron densities of the crystalline and amorphous phases are ρ_c and ρ_a, and the electron density difference between these phases is $\Delta\rho$. $\phi_{a,PCL}$ and $\phi_{a,PDLA}$ are the volume fraction of PCL and PDLA in the amorphous phase.

To understand how melt phase separation affects crystallization; consider that the crystallization in polymers can be described by primary (increase in x_S) and secondary (increase in x_L and x_{CL}) stages. The time variation of Q_{SAXS} and w_c is determined by the extent to which primary and secondary crystallization mechanisms contribute to increasing the crystallinity. For both blends, x_L (0.6) and x_{CL} (0.6) are constant during crystallization and independent of blend composition and melt phase separation time (t_{melt}) while the time variation of Q_{SAXS} and w_c during crystallization strongly depends on the extent of melt phase separation (Figure 2). Thus, during crystallization, w_c varies with x_S while Q_{SAXS} varies x_S and contrast between lamellar rich (x_L) and surrounding amorphous regions (1-x_L) as PCL crystallizes.

The fraction of PDLA in the amorphous phases (1-x_{CL} and 1-x_L) can be deduced from Q_{SAXS} /w_c(1- w_c). In 0.36 PCL, the fraction of PDLA (0.9) does not vary with $t_{melt.}$. In 0.50 PCL, the fraction of PDLA in the amorphous phase decreases from about 0.97 (t_{melt} = 0 h) to 0.65 (t_{melt} = 2 h) with melt phase separation. This decrease is consistent with the expulsion of PDLA to the

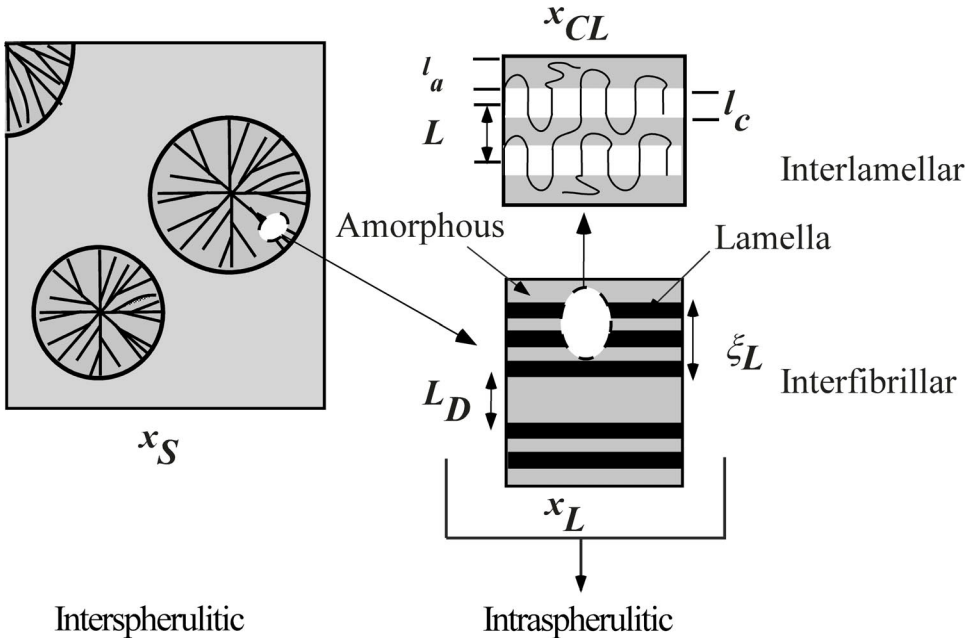

***Figure 1**: Schematic representation of the segregation of amorphous PDLA and uncrystallized PCL (dark regions) in PCL/PDLA blends. Structural variables characteristic of morphological level are x_S the volume fraction of spherulites, x_L the volume fraction of lamellar stacks and x_{CL} the fraction of crystals within lamellar stacks. Interlamellar morphological variables are* L, l_a, l_c *and interfibrillar variables are* ξ_L *and* L_D.

interspherulitic regions (1-x_S) as crystalline regions are enriched with PCL during melt phase separation, since the contrast between amorphous and crystalline PCL ($\Delta\rho$ = 0.043 moles electrons/cm^3) is less than that between crystalline PCL and PDLA ($\Delta\rho$ = 0.023 moles electrons/cm^3). Thus, even though the size of the interfibrillar amorphous regions (1-x_L) is controlled by the crystallization mechanism of PCL, the fraction of uncrystallized PCL and PDLA in these regions is controlled by melt phase separation.

In Figure 2, the crystallinity obtained at long times depends on melt phase separation. It must be noted that our experiments to times of 6000 s do not capture the complete long time evolution of the invariant and crystallinity for the blends. However, the approach to asymptotic limits is apparent at 6000 s. In order to obtain the ultimate crystallinity and the overall crystallization rate, the Avrami Equation [18,19] is applied [20] to w_c. For 0.36 PCL, the ultimate crystallinity for the nanophase separated blends can be reduced by 50 % following melt phase separation, while a smaller (30 %) reduction in the ultimate crystallinity (0.17) of nanophase separated 0.50 PCL can be obtained following melt phase separation. Although the crystallization rate of PCL is reduced by as much as 60 % in the one-phase blends, there is not a linear increase in this rate with melt phase separation, suggesting that the melt morphology also plays a role. Optical micrographs obtained for these blends qualitatively show that both blends exhibit interfibrillar segregation and support our conclusions from SAXS, since the coarser spherulite texture observed for 0.36 PDLA is due to a higher fraction of PDLA and uncrystallized PCL in the interfibrillar regions. Even when the blend sample is subsequently quenched to room temperature, the melt morphology determined the size and distribution of crystals as previously observed [8]. Our results clearly demonstrate that melt phase separation can be used to control the distribution of PDLA in the intraspherulitic and interspherulitic regions. Systematic studies are now necessary of how the mechanical properties, as well as the biological response of PDLA-rich regions can be controlled in PCL/PDLA blends tailored by melt phase separation. Our current research efforts are aimed in this direction.

Acknowledgements

SAXS and WAXS were carried out at the Advanced Polymer Beamline (X27C) at the National Synchrotron Light Source, Brookhaven National Laboratory. Y.A.A. would like to thank Dr. Feng-ji Yeh and Dr. Lizhi Liu for help with the synchrotron x-ray setup. J.C.M. gratefully recognizes support of the NRC/NIST Postdoctoral Research Fellowship.

References

[1] Mooney DJ, Park S, Kaufmann PM, Sano K, McNamara K, Vacanti JP, Langer R, J. Biomed. Mater. Res., **29**, 959-965, (1995).
[2] Marler JJ, Upton J, Langer R, Vacanti JP, Adv. Drug Deliv. Rev., **33**, 165-182, (1998).
[3] Langer R, J. Control. Release, **62**, 7-11, (1999).
[4] Vacanti CA, Vacanti JP, Langer R, ACS SYM SER, **540**, 16-34, (1994).
[5] Ikada Y, Tsuji H, Macromol. Rapid Commun., **21**, 117-132, (2000).
[6] Roe RJ, Rigby D, Adv. Polym. Sci., **82**, 103-139, (1987).
[7] Eastmond GC, Adv. Polym.Sci., **149**, 59-223, (1999).
[8] Meredith JC, Amis EJ, Macromol. Chem. Phys., **201**, 733-739, (2000).
[9] Strobl GR, Schneider M, J. Polym. Sci. Polym. Phys. Ed., **18**, 1343, (1980).
[10] Vonk CG, Pipers AP, J. Polym. Sci. Polym. Phys. Ed., **23**, 2517, (1985).

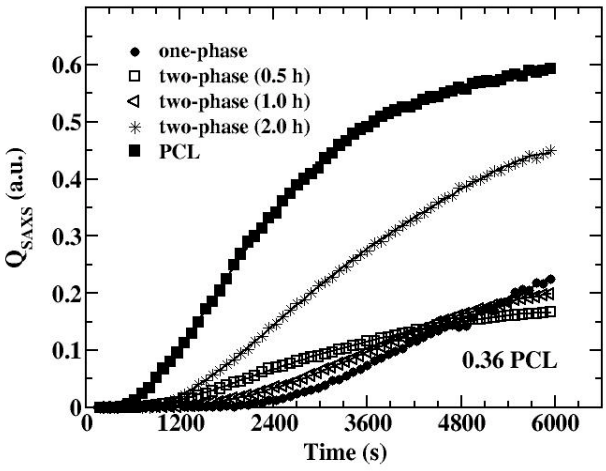

***Figure 2a**: Variation of Q_{SAXS} during crystallization of PCL and 0.36 PCL at 45 °C. Q_{SAXS} and w_c for PCL represent the crystallization of 0.36 PCL in the absence of PDLA.*

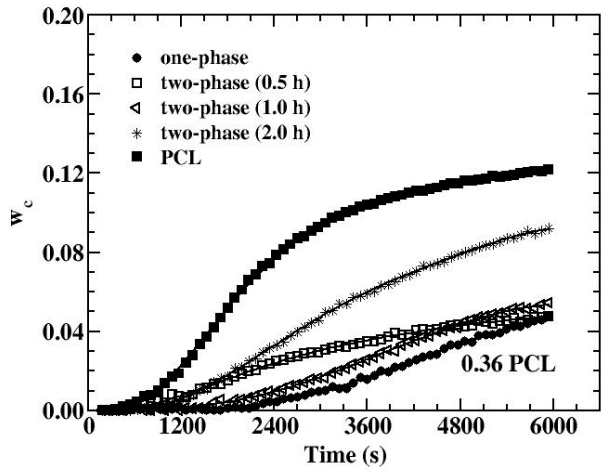

***Figure 2b**: Variation of w_c during crystallization of PCL and 0.36 PCL at 45 °C. Q_{SAXS} and w_c for PCL represent the crystallization of 0.36 PCL in the absence of PDLA.*

[11] Akpalu YA, Amis EJ, J. Chem. Phys., **113**, 392-403, (2000).
[12] Murthy NS, Akkapeddi MK, Orts WJ, Macromolecules, **31**, 142-152, (1998).
[13] Koberstein J, Russell TP, Stein RS, J. Polym. Sci. Polym. Phys. Ed., **17**, 1719-1730, (1979).
[14] Alexander LE: *X-ray Diffraction Methods in Polymer Science*. New York: Wiley; 1969.
[15] Chatani Y, Okita Y, Hiroyuki T, Yamashita Y, Polym. J., **1**, 555-562, (1970).
[16] Ryan AJ, Stanford JL, Bras W, Nye TMW, Polymer, **38**, 759-768, (1997).
[17] Akpalu YA, Amis EJ, J. Chem. Phys., **111**, 8686-8695, (1999).
[18] Avrami M, J. Chem. Phys., **7**, 1103, (1939).
[19] Avrami M, J. Chem. Phys., **9**, 177, (1941).
[20] Nojima S, Tsutsui H, Urushihara M, Kosaka W, Kato N, Ashida T, Polym. J., **18**, 451-461, (1986).

Tuning the Surfaces of Elastomers Through Mechanically Assembled Monolayers

J. Genzer and K. Efimenko
North Carolina State University

Tuning the surface characteristics of materials, including lubrication or wetting, has become of paramount interest for a variety of everyday applications. For example, while in some situations surfaces are required to be completely wettable (*i.e.*, the surfaces of metals before paint deposition), in other applications one needs to prevent the surfaces from being wettable. Examples of the latter include non-stick layers, marine anti-fouling coatings, surfaces of car windshields or frying pans, etc.

A typical way of adjusting materials surfaces is to deposit a self-assembled monolayer (SAM) of silane- or thiol-based molecules on the surfaces of silica or gold, respectively [1]. However, when exposed to polar liquids, such as water, these SAMs usually lose their low energy surface properties as the water molecules penetrate through the imperfections in the SAMs, causing this surface to reconstruct [2]. These non-desirable surface reconstruction effects can likely be minimized (or even completely prevented from occurring) by increasing the packing density of the SAMs through increasing the density of the grafting points at the surface. However, tailoring the grafting density of the SAM chains is not an easy task. SAMs are usually formed through self-assembly processes that are governed by the chemical and structural nature of the SAM molecules and the means of their attachment to the substrate. We have recently developed a method that enables us to control the grafting density of molecules anchored to surfaces [3]. Specifically, we demonstrated that the combination of the self-assembly with mechanical manipulation of the grafted molecules on surfaces provides a means of fabricating "mechanically assembled monolayers" (MAMs). We also showed that MAMs assembled from semifluorinated (SF) molecules form superhydrophobic surfaces with superior long-lasting barrier properties.

The method for fabricating MAMs made of $F(CF_2)_8(CH_2)_2SiCl_3$ (F8H2) molecules is schematically shown in the upper portion of Figure 1. The bottom part of Figure 1 shows the dependence of the advancing water contact angle, θ_w, of F8H2-MAM on the poly(dimethyl siloxane) (PDMS) substrate extension, Δx. The results in Figure 2 show that as Δx increases, θ_w increases (hydrophobicity of the surface increases) for both molecules and reaches a maximum at $\Delta x \approx 95\%$ and then decreases slightly for $\Delta x > 95\%$. The inset to Figure 2 shows the corresponding water contact hysteresis values (the difference between the advancing and receding water contact angles). The hysteresis decreases with increasing Δx, reaches a minimum at around $\Delta x \approx 60\%$, and then increases for $\Delta x > 70\%$. The results in Figure 2 indicate the packing of the F8H2 molecules in the F8H2-MAMs. As Δx increases from 0%, the number of the F8H2 groups per unit area increases, which in turn results in closer chain packing within the MAM. At $\Delta x \approx 60$ -70%, the molecules are already densely packed. With $\Delta x > 70\%$, the molecules in the MAM must begin to corrugate as a layer. This behavior gives rise to an enhanced molecular roughness and causes the contact angle hysteresis to increase.

We have designed a series of experiments aimed at exploring the resistance of the F8H2-MAMs to surface reconstruction. The samples were prepared as previously described, immersed in water for controlled

time intervals and subsequently dried with nitrogen. Figure 2 shows the advancing water contact angles, θ_w, of F8H2-MAMs prepared on PDMS-UVO substrates with Δx = 0% (solid symbols) and Δx = 70% (open symbols) after exposure to water. The θ_w on the F8H2-MAM fabricated on the unstretched substrate drops almost immediately after a short water exposure, which indicates that the F8H2 chains surface reconstruct. However, θ_w on the F8H2-MAM samples prepared on PDMS-UVO with Δx = 70% decreases only slightly with water exposure time. To check on the ability of the F8H2-MAMs to resist surface reconstruction, the samples were placed in a plastic Petri dish and left under ambient laboratory conditions (with no control of humidity or temperature) for six months. The crossed symbols in Figure 2 show the θ_w values measured on these samples. A close inspection of the data in Figure 2 reveals that during the six months "incubation" period the wettability of the F8H2-MAM samples decreased only by ≈ 3.5° for "as-prepared" samples and ≈ 5° for samples immersed in water for 7 days.

We used near edge x-ray absorption structure (NEXAFS) to study the molecular orientation of the MAMs surfaces [4]. NEXAFS involves the resonant x-ray excitation of a K or L shell electron to an unoccupied low-lying antibonding molecular orbital of σ symmetry, σ* (and π symmetry, π*). The initial state K shell excitation gives element specificity, while the final-state unoccupied molecular orbitals provides bonding or chemical selectivity [5]. Because of the fixed geometry and governing of the 1s → σ* (and 1s → π*) excitations by dipole selection rules, the resonance intensities vary as a function of the direction of the electric vector **E** of the incident polarized X-ray relative to the symmetry of the molecule [6]. The NEXAFS experiments were carried out on the NIST/Dow soft x-ray materials characterization facility (beamline U7A) at the National Synchrotron Light Source at Brookhaven National Laboratory (NSLS BNL) [7]. The set-up at NSLS BNL is capable of measuring both the partial electron yield (PEY) NEXAFS and the fluorescence yield (FY) NEXAFS spectra. By simultaneously detecting both the PEY and FY NEXAFS signals, whose probing depths are ≈ 2 and ≈100 nm, respectively, the orientation of the molecules on the surface and in the interior of the sample can be resolved.

No measurable fluorine signal could be detected in the FY NEXAFS spectra of the SF-MAMs, suggesting that the UVO treatment and subsequent MAMs deposition did not modify the interior of the PDMS. On the other hand, the PEY NEXAFS data revealed a strong peak at 292.0 eV, corresponding to the 1s → σ^*_{CF} [4]. Figure 3 shows the PEY NEXAFS spectra collected from F8H2-MAM samples with Δx = 0% and Δx = 70%. PEY NEXAFS spectra taken in the direction parallel (upper spectra) and perpendicular (lower spectra) to the stretching direction are shown for both samples. In all cases the PEY NEXAFS spectra were collected at the normal (θ = 90°) and grazing (θ = 20°) incidence geometries, where q is the angle between the sample normal and the polarization vector of the x-ray beam. By inspecting the PEY NEXAFS signals, several characteristic peaks can be identified that correspond to the 1s → σ* transitions associated with the C-H (E = 287.0 eV), C-F (E = 292.0 eV), and C-C (E = 295.5

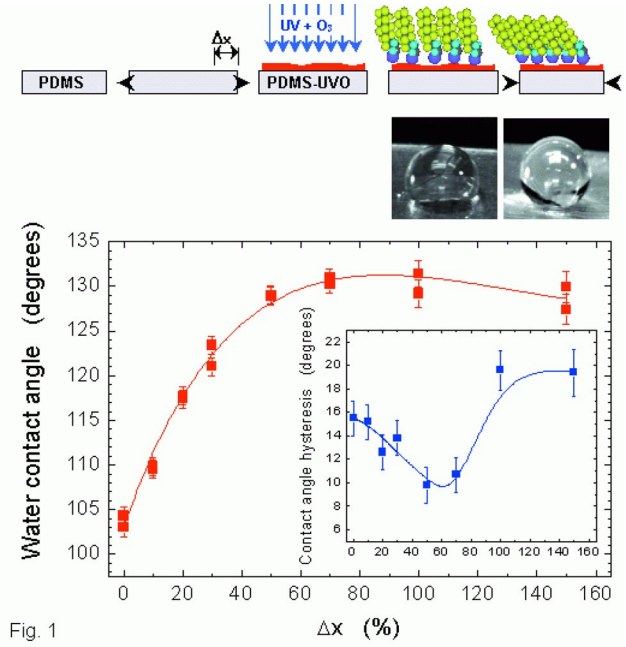

Fig. 1

Figure 1 The upper part shows a schematic illustrating the technological steps leading to the production of "mechanically assembled monolayers" (MAMs). First, a pristine poly(dimethyl siloxane) (PDMS) network film is prepared. After soxhlet extraction in chloroform for 24 hours, which removed any non-cross-linked oligomers, the film is cut into small strips (≈ 1 x 5 cm²) and mechanically stretched by a certain length, Δx. Subsequent exposure to an ultraviolet/ozone (UVO) treatment produces hydrophilic PDMS surfaces (PDMS-UVO) composed mainly of hydroxyl groups. The semifluorinated (SF) chlorosilane molecules, $F(CF_2)_8(CH_2)_2SiCl_3$ (F8H2), are deposited from vapor onto this stretched substrate and form an organized SAM. Finally, the strain is released from the PDMS-UVO film, which returns to its original size, causing the grafted F8H2 molecules to form a densely packed MAM. To remove weakly physisorbed F8H2 molecules the samples are thoroughly washed in warm (≈ 60°C) distilled water for 1 minute and dried with nitrogen. The lower part denotes the dependence of water contact angle, θ_w, on F8H2-MAM samples on Δx. The inset shows the corresponding contact angle hysteresis (defied as the difference between the advancing and receding water contact angles). The lines are meant to guide the eye. Also shown are photographs of a water droplet spreading on the F8H2-MAM (Δx=0%) and F8H2-MAM (Δx=70%) surfaces.

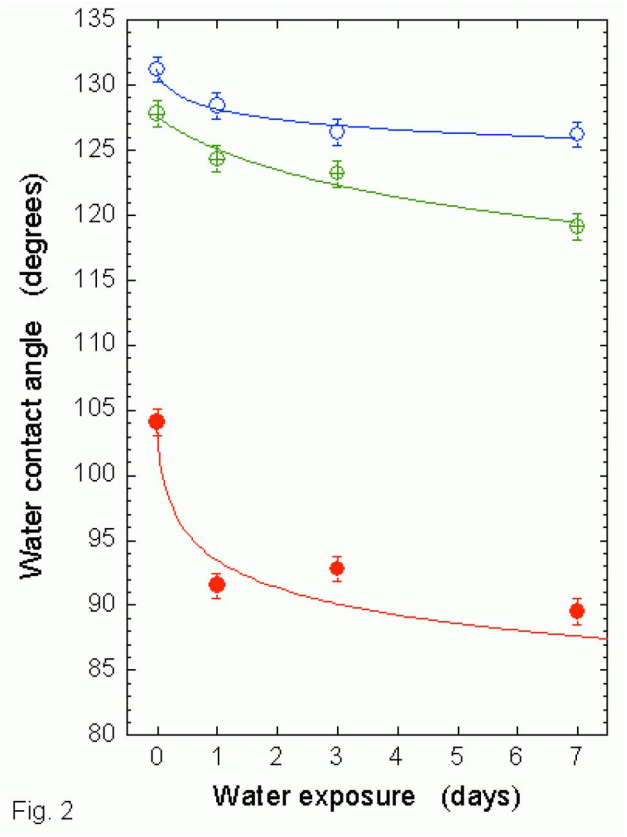

Fig. 2

Figure 2 The dependence of water contact angle, θ_w, on the exposure time of F8H2-MAM to water. The solid symbols denote the contact angles measured on F8H2-MAMs with Δx = 0%. The open symbols mark the contact angles measured on F8H2-MAMs with Δx = 70% taken immediately after the water exposure and substrate drying with nitrogen. The crossed symbols represent the contact angles from the samples denoted by the open symbols but measured 6 months later (the samples were stored under ambient laboratory condition in Petri dishes with no temperature or humidity control between the water exposure and the measurement). The lines are meant to guide the eye.

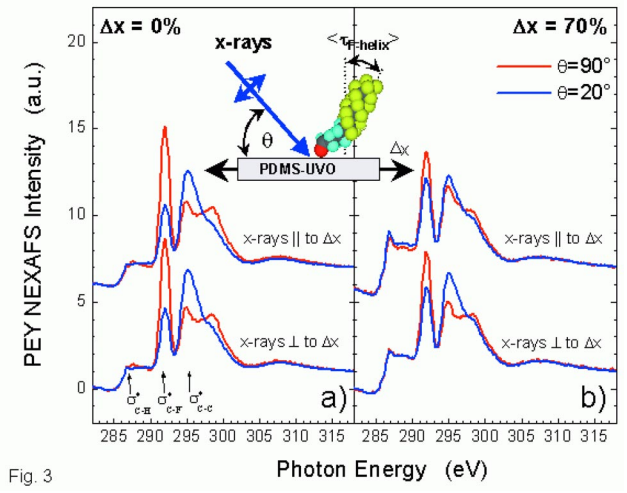

Fig. 3

Figure 3 The partial electron yield (PEY) NEXAFS spectra at the C edge of F8H2-MAMs deposited on PDMS-UVO substrates that were not stretched (Figure 3a), and stretched to Δx = 70% (Figure 3b) before the UVO treatment. The red and blue lines denote the PEY NEXAFS spectra taken at the normal (θ = 90°) and grazing (θ = 20°) incidence, respectively, geometries of the X-ray beam along (upper spectra) and perpendicular to (lower spectra) the stretching direction. The arrows indicate the positions of the 1s → σ transitions associated with the C-H (E = 287.0 eV), C-F (E = 292.0 eV), and C-C (E = 295.5 eV) bonds. The inset shows schematically the set-up geometry.*

eV) bonds. The fact that the intensities originating from these transitions change with varying angle θ (as θ increases the intensity corresponding to σ* of the C-F bond increases, while that of the C-C bond decreases) indicates that the samples are oriented. The orientation of the F8H2 molecules can be inferred by qualitatively examining the PEY NEXAFS data. The $\sigma^*_{C\text{-}F}$ signal in the NEXAFS spectra collected at θ = 90° is always stronger than that measured at θ = 20°; thus the director of the F8H2 molecule is only slightly tilted away from the sample normal. A more quantitative analysis using models presented elsewhere [4] reveals that the average tilt angles of the fluorocarbon helix [8], $\langle\tau_{F\text{-}helix}\rangle$, measured along and perpendicular to the stretching direction on the F8H2-MAM sample prepared on unstretched PDMS-UVO substrate, are ≈ 5° and ≈ 4°, respectively. Thus, the F8H2 molecules are oriented almost perpendicular to the PDMS-UVO substrate, which is in accord with the orientation of F8H2-SAM deposited on a SiO_x substrate [4]. The analysis of the PEY NEXAFS spectra from F8H2-MAM with Δx = 70% reveals that $\langle\tau_{F\text{-}helix}\rangle$ measured along the stretching direction is ≈ 38° and $\langle\tau_{F\text{-}helix}\rangle$ collected perpendicular to the stretching direction is 21°. The NEXAFS experiments thus show clearly that as Δx increases, the F8H2 chains tilt away from the sample normal in the stretching direction. The fact that $\langle\tau_{F\text{-}helix}\rangle$ increases from ≈ 4° to ≈ 21° as Δx increases from 0% to 70% can be attributed to the slight compression of the sample perpendicular to the uniaxial stretch.

Figure 4 shows the values of the average tilt angles of the fluorocarbon helix, $\langle\tau_{F\text{-}helix}\rangle$, that were determined from PEY NEXAFS spectra collected from F8H2-MAMs with Δx = 0% (squares) and Δx = 70% (circles). As mentioned earlier in this report, the F8H2-MAMs prepared on unstretched PDMS-UVO substrates (Δx = 0%) stand almost perpendicular to the sample surface. However, the data in Figure 4 shows that when exposed to water, the chain orientation starts to disappear very rapidly and after about 1 day of water expo-

sure, the F8H2-MAMs with $\Delta x = 0\%$ disorient completely. The behavior of the F8H2-MAMs prepared on PDMS-UVO substrates with $\Delta x = 70\%$ is very different. Specifically, the NEXAFS data reveal that $<\tau_{F\text{-}helix}>$ on samples exposed to water for up to 7 days is indistinguishable from that measured on the same specimen before the water exposure. These results thus provide further evidence that the F8H2 molecules in MAMs with $\Delta x = 70\%$ are closely packed and mechanically interlocked; this interlocking hinders the chain's tendency to move and reconstruct on the MAM surface. We attribute this unusual behavior to the extremely high packing densities of the MAMs.

This research was supported by the NCSU COE start-up funds and the NSF CAREER award to J.G., Grant No. DMR98-75256. NEXAFS experiments were carried out at the National Synchrotron Light Source, Brookhaven National Laboratory, which is supported by the U. S. Department of Energy, Division of Materials Sciences and Division of Chemical Sciences. The authors thank Daniel Fischer and William Wallace (both NIST) for their assistance during the course of the NEXAFS experiments.

References and Notes

[1] A. Ulman, An Introduction to Ultrathin Organic Films from Langmuir-Blodgett to Self Assembly, (Academic Press: New York, 1991); M. K. Chaudhury, Mat. Sci. Eng. Rep. **1996**, *16*, 97.
[2] J. Wang *et al.*, Macromolecules **30**, 1906 (1997).
[3] J. Genzer, K. Efimenko, Science, 290, 2130 (2000).
[4] J. Genzer *et al.*, Langmuir **16**, 1993 (2000); J. Genzer *et al.*, Macromolecules **33**, 1882 (2000).
[5] J. Stöhr, NEXAFS Spectroscopy, (Springer-Verlag: Berlin, 1992).
[6] Due to the nature of the polarization dependencies of the NEXAFS signal intensities one cannot distinguish between a completely disoriented sample and a sample, whose chains are all tilted by 54.7°, the so called, "magic angle" [5].
[7] D. A. Fischer *et al.*, Appl. Surf. Sci. **133**, 58 (1998).
[8] We note that the tilt angle determined from NEXAFS represents an *average* value. There is no straightforward way to discriminate between the case of all chains homogeneously tilted by the same angle and the case of a disordered system with a broad distribution of tilt angles. Hence, we express our results on the orientation of the SF moieties in terms of the average tilt angle of the fluorocarbon part of the single SF groups, $<\tau_{F\text{-}helix}>$.

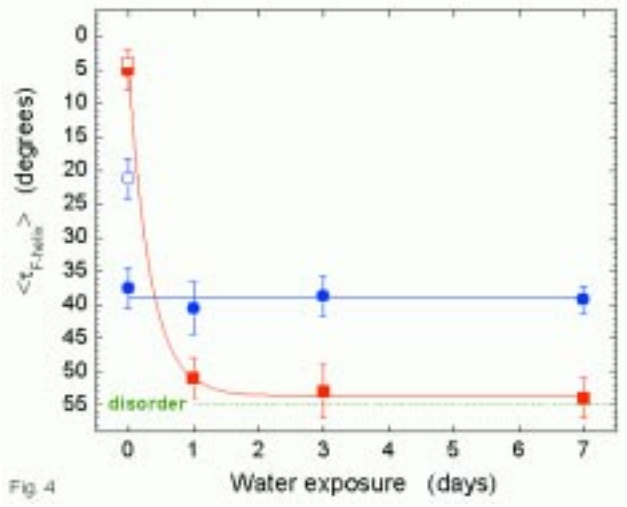

Figure 4 The dependence of the average tilt angle of the fluorinated helix, $<\tau_{F\text{-}helix}>$, in F8H2-MAMs on the exposure time of the F8H2-MAM to water. The squares and circles denote $<\tau_{F\text{-}helix}>$ in F8H2-MAM ($\Delta x = 0\%$) and F8H2-MAM ($\Delta x = 70\%$) samples. The solid and open symbols represent $<\tau_{F\text{-}helix}>$ measured along and perpendicular to, respectively, the stretching direction. The dashed line marks the value of $<\tau_{F\text{-}helix}>$ corresponding to a completely disoriented MAM. The solid lines are meant to guide the eye.